



GravPSO2D: A Matlab package for 2D gravity inversion in sedimentary basins using the Particle Swarm Optimization algorithm

J.L.G. Pallero, J.L. Fernández-Martínez, Z. Fernández-Muñiz, Sylvain Bonvalot, Germinal Gabalda, Thierry Nalpas

► To cite this version:

J.L.G. Pallero, J.L. Fernández-Martínez, Z. Fernández-Muñiz, Sylvain Bonvalot, Germinal Gabalda, et al.. GravPSO2D: A Matlab package for 2D gravity inversion in sedimentary basins using the Particle Swarm Optimization algorithm. *Computers & Geosciences*, 2021, 146, pp.104653. 10.1016/j.cageo.2020.104653 . insu-02998258

HAL Id: insu-02998258

<https://insu.hal.science/insu-02998258>

Submitted on 10 Nov 2020

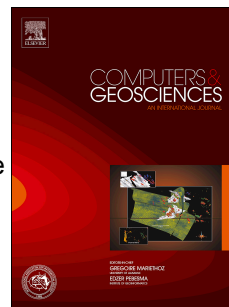
HAL is a multi-disciplinary open access archive for the deposit and dissemination of scientific research documents, whether they are published or not. The documents may come from teaching and research institutions in France or abroad, or from public or private research centers.

L'archive ouverte pluridisciplinaire **HAL**, est destinée au dépôt et à la diffusion de documents scientifiques de niveau recherche, publiés ou non, émanant des établissements d'enseignement et de recherche français ou étrangers, des laboratoires publics ou privés.

Journal Pre-proof

GravPSO2D: A Matlab package for 2D gravity inversion in sedimentary basins using the Particle Swarm Optimization algorithm

J.L.G. Pallero, J.L. Fernández-Martínez, Z. Fernández-Muñiz, S. Bonvalot, G. Gabalda, T. Nalpas



PII: S0098-3004(20)30629-4

DOI: <https://doi.org/10.1016/j.cageo.2020.104653>

Reference: CAGEO 104653

To appear in: *Computers and Geosciences*

Received Date: 17 February 2020

Revised Date: 23 October 2020

Accepted Date: 28 October 2020

Please cite this article as: Pallero, J.L.G., Fernández-Martínez, J.L., Fernández-Muñiz, Z., Bonvalot, S., Gabalda, G., Nalpas, T., GravPSO2D: A Matlab package for 2D gravity inversion in sedimentary basins using the Particle Swarm Optimization algorithm, *Computers and Geosciences* (2020), doi: <https://doi.org/10.1016/j.cageo.2020.104653>.

This is a PDF file of an article that has undergone enhancements after acceptance, such as the addition of a cover page and metadata, and formatting for readability, but it is not yet the definitive version of record. This version will undergo additional copyediting, typesetting and review before it is published in its final form, but we are providing this version to give early visibility of the article. Please note that, during the production process, errors may be discovered which could affect the content, and all legal disclaimers that apply to the journal pertain.

© 2020 Published by Elsevier Ltd.

GRAVPSO2D: A Matlab package for 2D gravity inversion in sedimentary basins using the Particle Swarm Optimization algorithm

J.L.G. Pallero^{a,*}, J.L. Fernández-Martínez^b, Z. Fernández-Muñiz^b, S. Bonvalot^c, G. Gabalda^c, T. Nalpas^d

^a*ETSI en Topografía, Geodesia y Cartografía. Universidad Politécnica de Madrid. Madrid, Spain*

^b*Grupo de Problemas Inversos, Optimización y Aprendizaje Automático. Departamento de Matemáticas. Universidad de Oviedo, Oviedo, Spain*

^c*GET (Université de Toulouse, CNRS, IRD, CNES) - Bureau Gravimétrique International (BGI), Toulouse, France*

^d*Univ Rennes, CNRS, Géosciences Rennes, UMR 6118, 35000 Rennes, France*

Abstract

In this paper GRAVPSO2D, a Matlab tool for two-dimensional gravity inversion in sedimentary basins using the Particle Swarm Optimization (PSO) algorithm, is presented. The package consists of a collection of functions and scripts that cover the main three parts of the process: (1) the model definition based on the observations, (2) the inversion itself, where the PSO is employed, and (3) the results processing, including best model estimation, uncertainty analysis and plots generation. GRAVPSO2D is freely available, and represents an effort for providing

*Corresponding author

Email addresses: jlg.pallero@upm.es (J.L.G. Pallero), jlfm@uniovi.es (J.L. Fernández-Martínez), zulima@uniovi.es (Z. Fernández-Muñiz), sylvain.bonvalot@ird.fr (S. Bonvalot), germinal.gabalda@ird.fr (G. Gabalda), thierry.nalpas@univ-rennes1.fr (T. Nalpas)

Author contributions: J.L.G.P., J.L.F.M., and Z.F.M. designed the methodology, developed the software, processed the data, and wrote the paper. G.G., and T.N. acquired the gravity data. S.B., G.G., and T.N. analyzed, discussed the inversion results corresponding to the real example, and wrote the related part of the paper.

the scientific community with the first tool based on the PSO algorithm in order perform the inversion and the uncertainty assessment of the sedimentary basin gravity inversion problem, taking into account the gravity regional trend estimation, and vertically and horizontally density contrast variations. Synthetic and real examples are provided in order to show the software capabilities.

Keywords: Nonlinear gravity inversion, Particle Swarm Optimization, Uncertainty assessment, Sedimentary basin

1. Introduction

2 The interface separation between two media having different densities can be
 3 estimated in Geophysics using gravity measurements and by posing a nonlinear
 4 inverse problem. Gravity inversion in this kind of environments is a tool fre-
 5 quently used in Geophysics in tasks such as prospecting of oil and gas, or in hydro-
 6 geology and glaciology studies (Blakely, 1995; Dobrin, 1960; Hinze et al., 2013;
 7 Nettleton, 1976; Parker, 1994; Telford et al., 1976). The gravity inverse problem
 8 has a non-unique solution, leading to an infinity number of solutions (Al-Chalabi,
 9 1971; Skeels, 1947; Zhdanov, 2015). It is therefore mandatory to introduce some
 10 kind of regularization and/or constraint(s) incorporating other **geophysical** infor-
 11 mation such as borehole and seismic profile data, contrasted prior models, etc.
 12 This will allow to restrict the set of possible solutions and stabilize the inversion.

13 The problem of the estimation of the basement relief in sedimentary basins
 14 using gravity observations is a nonlinear inverse problem, and the most used tech-
 15 niques for its solution are based on local optimization methods, either by the lin-
 16 earization of the problem plus regularization (see Silva et al. (2009) for example),
 17 or by the sequential application of the direct formulation (see Bott (1960) or Chen

¹⁸ and Zhang (2015) for example). GRAVPSO2D uses Particle Swarm Optimization
¹⁹ (PSO), which is a global search method with excellent capabilities to perform the
²⁰ inverse problem uncertainty analysis and avoiding the weak points of the local
²¹ optimization procedures, such as the dependency on the prior model and the lack
²² of a proper uncertainty analysis (Fernández-Martínez et al., 2013, 2014b).

²³ GRAVPSO2D works in two-dimensional environments. This approximation
²⁴ can be used when the dimension of an anomalous body is much larger than the
²⁵ other two dimensions (at least a 4× or 6× factor according to Nettleton (1976)).
²⁶ This situation is common in sedimentary basins, where their horizontal extensions
²⁷ are generally much larger than their depth, so profiles perpendicular to the princi-
²⁸ pal dimensions can be used for the analysis in a 2D formulation (Pick et al., 1973;
²⁹ Telford et al., 1976).

³⁰ 2. Observations and basin modelization

³¹ GRAVPSO2D works with user-provided complete Bouguer gravity anomalies,
³² Δg , along a profile. The software can also estimate a polynomial regional trend
³³ during the inversion, so if this effect exists in Δg it is not necessary to be previously
³⁴ suppressed by the user.

³⁵ The 2D basin modeling used in GRAVPSO2D consists in the juxtaposition of
³⁶ rectangles along the profile as it was commonly employed by other authors (see
³⁷ for example Silva et al. (2009) or Ekinci et al. (2020)). As it can be seen in
³⁸ Fig. B.1, the rectangles' upper sides are located at the surface level (considered
³⁹ plane in the figure, although that is not mandatory, so they can be adapted to the
⁴⁰ terrain topography). It is common to set the horizontal dimensions to be equal
⁴¹ for all rectangles, but GRAVPSO2D can also work with unequal widths. Then, the

⁴² bottom sides depict the sediments-basement interface.

FIGURE B.1 HERE (ONE COLUMN WIDTH)

⁴³ Let N be the number of observed gravity points, $P_i(l_i, z_i)$, with $i = 1 \dots N$, and
⁴⁴ where l_i is the point position along the profile length, and z_i the point height. The
⁴⁵ gravity residual anomaly generated over each point by a model composed of M
⁴⁶ rectangles follows the equation

$$\Delta g_{P_i}^r = \sum_{j=1}^M F(\Delta\rho(z_j), z_j, \mathbf{r}_{ij}), \quad (1)$$

⁴⁷ where F is the forward operator (see [Appendix A](#)), $\Delta\rho(z_j)$ is the particular rect-
⁴⁸ angle density contrast, constant or variable with depth, z_j is the particular rectan-
⁴⁹ gle bottom side height (the problem unknowns), and \mathbf{r}_{ij} is the position vector of
⁵⁰ each rectangle related to each observation point. If a polynomial regional trend
⁵¹ is added, which contributes with the anomaly Δg^t , the gravity anomaly over each
⁵² observation point is:

$$\begin{aligned} \Delta g_{P_i} &= \Delta g_{P_i}^r + \Delta g_{P_i}^t \\ &= \sum_{j=1}^M \left[F(\Delta\rho(z_j), z_j, \mathbf{r}_{ij}) + \sum_{k=D}^0 A_k (l_i - l_r)^k \right], \end{aligned} \quad (2)$$

⁵³ where D is the polynomial degree, A_k are the polynomial coefficients, and l_r is a
⁵⁴ reference position.

⁵⁵ In real environments sediments' density typically increases with depth, so the
⁵⁶ density contrast sediments-basement, $\Delta\rho$, decreases. GravPSO2D can work with
⁵⁷ both, constant or variable density contrast. In the latter case, this variation can be
⁵⁸ vertical (with depth), and also horizontal.

⁵⁹ Many models of density contrast variation with depth have been used in the lit-
⁶⁰ erature. Constant values are frequently used ([Barbosa et al., 1997, 1999](#)), but vari-

able density contrast is also very common: Rao (1990) used a quadratic equation,
 Chakravarthi and Sundararajan (2007) a parabolic law, Litinsky (1989); Silva et al.
 (2006) a hyperbolic law, and Parker (1972); Granser (1987); Pham et al. (2018) an
 exponential law. All these models produce complicated equations hard to manage
 that do not match well the density variation with depth in some real environments
 (see for example density logs in Brocher (2005) or Silva et al. (2006)).
 In order to manage the vertical density contrast variation, GRAVPSO2D can
 use a piecewise model, having the advantages of (1) any density variation can be
 used, and (2) only the formulation corresponding to the constant density model
 (Eq. (A.1)) is needed. An example can be seen in Fig. B.2, where a constant value
 of $\Delta\rho = -600 \text{ kg m}^{-3}$ is used between depths from 0 m to 100 m; then, a linear
 variation from $\Delta\rho = -570 \text{ kg m}^{-3}$ to $\Delta\rho = -520 \text{ kg m}^{-3}$ is used between depths
 100 m to 150 m, and finally a constant value of $\Delta\rho = -520 \text{ kg m}^{-3}$ is employed for
 depths greater than 150 m. GRAVPSO2D divides each subsoil model's rectangle
 based on the density profile for computing the whole attraction, and uses constant
 density sub-rectangles of user-defined size to approximate the zones with density
 variation.

FIGURE B.2 HERE (ONE COLUMN WIDTH)

GRAVPSO2D can also manage horizontal density contrast distributions. In this
 case the gravity profile is divided into horizontal sectors, and different vertical
 density contrast models are assigned to each one. All these configurations are
 provided via text files.

82 **3. Particle Swarm Optimization**

83 The PSO (Particle Swarm Optimization) algorithm ([Kennedy and Eberhart, 1995](#)) is a global optimizer based on the behavior of swarms of animals (birds, 84 fish schools) in the nature searching for food. A set of particles (models) explores 85 the parameters' space with the goal of the optimization of a given cost function 86 related to the inverse problem that is considered. As general overview, the algo- 87 rithm works as follows: (1) in the first step, a set of particles (models) is created 88 with random positions (the problem parameters) and velocities, and the objective 89 function is employed to determine the fitness of each model in the set, (2) as time 90 passes, the particles' position and velocity are updated based on their fitness and 91 the corresponding values of their neighbors, i. e., the behavior of an individual is 92 influenced by its own experience and that of its neighbors ([Fernández-Martínez 93 et al., 2008](#)).

95 The algorithm depends internally of a set of parameters, where the more im- 96 portant are the so-called *inertia weight*, and *local* and *global accelerations*. Mod- 97 ifying how the velocities and accelerations of the particles are described a family 98 of PSO variants are describable, and among them GRAVPSO2D can use the so-called 99 GPSO, CC-PSO, CP-PSO, PC-PSO, PP-PSO, PR-PSO, RC-PSO, RP-PSO and 100 RR-PSO family members ([Fernández-Martínez and García-Gonzalo, 2009, 2012; 101 García-Gonzalo et al., 2014](#)). The cloud versions of these algorithms are used, 102 i. e., no parameter tuning of inertia nor accelerations must be configured by the 103 user, given that each the particle has its own PSO parameters, automatically cho- 104 sen ([García-Gonzalo and Fernández-Martínez, 2009](#)).

105 Pioneer applications of PSO in the field of applied geophysics can be seen in 106 [Fernández-Álvarez et al. \(2006\); Fernández-Martínez et al. \(2010a,b\); Shaw and](#)

107 Srivastava (2007). In Fernández-Martínez et al. (2010a), for example, an applica-
 108 tion of PSO to a 1D-DC resistivity inverse problem is presented. More recently,
 109 in Luu et al. (2018) an application to the seismic travelttime tomography problem
 110 can be seen, and in Li et al. (2019) PSO is applied to microseismic location. Nev-
 111 ertheless, in gravity and other potential field inversion methods the PSO algorithm
 112 has been barely used (Essa and Elhussein (2018), for example, apply PSO in the
 113 inversion of magnetic anomalies generated by simple structures).

114 In Sanyi et al. (2009) several simple gravity synthetic examples based on
 115 buried cylinders are solved using PSO, comparing the obtained results with other
 116 global search methods (genetic algorithms, simulated annealing, and ant colony
 117 optimization), and also with a classical Levenberg-Marquardt approach. In Tou-
 118 shmalani (2013a,b) PSO was employed to estimate the parameters of a fault based
 119 on gravity anomaly observations. The conclusion of the study is that PSO provides
 120 better agreement between the estimated and the synthetic model anomaly than the
 121 classical approach using linearization and the Levenberg-Marquardt method. In
 122 Roshan and Singh (2017) PSO is employed in the gravity inversion of a spher-
 123 ical and a vertical cylindrical models, as well as its application to a real exam-
 124 ple (modeled as a vertical cylinder). In all these papers PSO is employed as a
 125 global optimizer, and performance tests are performed in most cases against local
 126 optimization techniques. But the most important feature of global optimization
 127 algorithms is missed: their capability to perform an approximate nonlinear uncer-
 128 tainty analysis of the inverse solution by the sampling of the nonlinear uncertainty
 129 region(s). Few papers were found (Singh and Biswas, 2016; Ladino and Bassrei,
 130 2016) where the inversion uncertainty is analyzed using the frequency distribution
 131 of the model parameters and/or cross-plots of parameters. In Fernández-Muñiz

132 et al. (2020) an application of PSO to gravity inversion of isolated anomalous
 133 bodies plus uncertainty assessment using PSO can also be seen.

134 In Pallero et al. (2015, 2017), first attempts to apply the PSO algorithm to the
 135 gravity inverse problem in sedimentary basins were presented for 2D and 3D envi-
 136 ronments, respectively. In Ladino and Bassrei (2016) a mixed model of PSO plus
 137 regularized Gauss-Newton method is employed for 3D gravity inverse problem
 138 in sedimentary basins, where PSO provides the initial model for a final Gauss-
 139 Newton inversion and cross-plots are employed for uncertainty analysis. In Singh
 140 and Singh (2017) PSO is applied to a 2.5D gravity inversion in sedimentary basins,
 141 although in this case only comparisons with results obtained via the Marquardt
 142 method are performed. Finally, Ekinci et al. (2020) have recently used a different
 143 global optimization method, called *differential evolution algorithm* (DEA), to a
 144 2D approximation of this kind of problem applied to the Aegean Graben System
 145 (Turkey), performing algo uncertainty analysis.

146 4. The 2D basement relief gravity inverse problem and PSO

147 In this section a general overview about the 2D basement relief gravity inverse
 148 problem in the frame of the PSO algorithm is presented. The main configuration
 149 parameters and other details are enumerated and explained.

150 The first important parameters to impose for the PSO execution are the search
 151 space limits, which are established based on a first approximation model esti-
 152 mated using the Bouguer's plate formulation. It is important to stress that this
 153 first approximation model does not act as the initial model in the local optimiza-
 154 tion methods, but it is only a guidance for the PSO search bounds determination,
 155 therefore not much accuracy is needed (this topic is explained in detail in the

156 GRAVPSO2D reference manual). Then, other important parameters to select are
 157 the swarm size and the number of iterations. At each iteration, a number of mod-
 158 els equal to the swarm size are generated, i. e., the search space is sampled during
 159 the PSO execution. After each iteration the cost function value for each model is
 160 computed, which is a value that has influence in the posterior swarm evolution.
 161 This cost function is defined as

$$c = \frac{\|\mathbf{v}\|_p}{\|\mathbf{o}\|_p} \cdot 100, \quad (3)$$

162 where p is a user-selected vector norm. In the last step of the algorithm all gener-
 163 ated models are analyzed according to their cost function values.

164 The vector \mathbf{o} is defined as

$$\mathbf{o} = \Delta\mathbf{g}^o - \Delta\mathbf{g}^t, \quad (4)$$

165 i. e., the vector of observed gravity anomaly minus the regional trend values (if
 166 they are estimated during the inversion or imposed). The vector \mathbf{v} is defined as

$$\mathbf{v} = \Delta\mathbf{g}^o - \Delta\mathbf{g}^t - \Delta\mathbf{g}^r, \quad (5)$$

167 i. e., the vector of observed gravity anomaly minus the regional trend values (if
 168 they are estimated during the inversion or imposed) minus the residual gravity
 169 generated by the corresponding subsoil model in the swarm. If the observations
 170 have an associated standard deviation information, it can be used in GRAVPSO2D
 171 for weighting the cost function computation.

172 Other important aspect in GRAVPSO2D is model filtering. The direct applica-
 173 tion of global search algorithms to the sedimentary basin gravity inverse problem
 174 produces unrealistic models characterized by a sawtooth profile (Boschetti et al.,

175 1997; Parker, 1999; Pallero et al., 2015). This can be mitigated via a moving av-
 176 erage filtering applied to the generated PSO models, and prior to the computation
 177 of the pertinent cost function value. Filtering is in this case the way to introduce
 178 relative constraints (Barbosa et al., 1997) in the problem, and the use of aver-
 179 age filtering technique permits a flexible configuration of the method behavior for
 180 different values in the filtering window.

181 Finally, using absolute constraints (Barbosa et al., 1997) is also possible. Ab-
 182 solute constraints are values of sediments-basement interface depths (or minimum
 183 depths) that can come from boreholes, seismic profiles or other sources. These
 184 data can be used to fix (or permit a small variation around a value) the depth value
 185 of parts of the subsoil model and its surroundings.

186 5. The GravPSO2D package

187 The GravPSO2D package is a Matlab software, so it is possible to work with
 188 it in any operating system where Matlab¹ is present.

189 5.1. Package organization and installation

190 Once the user has downloaded and uncompressed the package, a folder called
 191 grav-ps0-2d/ will be obtained. This folder contains the following elements:

- 192 • A folder called pso_programs_v3/ containing the Particle Swarm Opti-
 193 mization code.

¹Matlab 9.2.0.538062 (R2017a) Linux version (under Debian GNU Linux) was employed in the writing of the software, but, as no special packages nor extensions are used, any version should be capable to execute GravPSO2D.

- 194 • A folder called doc/ that stores a complete and self-contained 61-page ref-
 195 erence manual.
- 196 • A folder called examples/ containing the example data.
- 197 • A collection of 14 files whose names follow the template grav2d_* .m.

198 *5.2. Main scripts*

199 On the user side, GRAVPSO2D is composed by three main scripts, which are:

- 200 • `grav2d_ModelDefinition.m`. This script helps to prepare the data prior
 201 to the inversion. Based on the observations data file and several user con-
 202 figuration variables, this script performs the subsoil partition.
- 203 • `grav2d_Inversion.m`. This script performs the inversion using the PSO
 204 algorithm. The user can select several parameters, such as the PSO fam-
 205 ily member, the swarm size and the number of iterations, the activation of
 206 weights, the vector norm for the cost function evaluation, and others. As
 207 a result, the script generates a file containing, among other internal infor-
 208 mation, all the sampled models, which will be the data to use in the post
 209 processing stage.
- 210 • `grav2d_Plot.m`. This script analyzes the results obtained by `grav2d_Inversion.m`,
 211 providing the inversion results in text and graphical modes, which can be
 212 configured by the user through some variables.

213 *5.3. Input data files*

214 In this section, the different input data files will be enumerated (a detailed
 215 description of the different formats is stated in the user's manual). All input data

216 files used by GRAVPSO2D are ASCII files, so it can be opened and edited by any
217 text editor.

218 • **Observations data file.** The observations data file contains a gravity profile
219 in rectangular coordinates, and is the fundamental file in GRAVPSO2D.

220 • **Subsoil data file.** This file describes the subsoil partition in rectangles,
221 which is the model used by the software, as it was described in section 2.

222 • **Regional trend data file.** If the user wants to use a regional trend in inver-
223 sion (estimation or only using a predefined one), a first approximation must
224 be introduced via a configuration file. This first approximation does not act
225 as initial approximation as in local optimization algorithms, but only as a
226 reference to compute the search space **for the polynomial coefficients** in the
227 PSO algorithm.

228 • **Density contrast definition data files.** Two files can be configured related
229 to this topic, one for the vertical, and one for the horizontal density contrast
230 variations. In the former case, the vertical variation is configured piecewise
231 providing information about depths and the corresponding density contrast.
232 Multiple configurations can be defined, each one marked by an identifier. In
233 the case of the horizontal density distribution the corresponding file stores a
234 set of segments, and a vertical contrast density configuration is assigned to
235 each of them via the identifier.

236 • **Filtering data file.** For the filtering step the user must provide the window
237 filter coefficients, which are stored in a file and can be freely selected.

- 238 • **Boreholes data file.** In this file borehole information is stored. The user
 239 can configure a fixed value or an influence area for a prescribed basement
 240 depth.

241 *5.4. Output files*

242 The `grav2d_Inversion.m` script generates after its execution a unique file,
 243 stored as Matlab `*.mat` format (version 7), containing the inversion's results. It
 244 contains a structure comprising all the generated models during the PSO execu-
 245 tion, as well as all the inversion details (an in-depth description of the structure
 246 is presented in the GRAVPSO2D reference manual). This file is loaded by the
 247 `grav2d_Plot.m` in order to generate its results.

248 **6. Synthetic example**

249 In this section a synthetic example is presented in order to illustrate the behav-
 250 ior of the GRAVPSO2D software. A synthetic subsoil composed by 126 rectangles
 251 of 200 m horizontal width with upper sides from height 976 m to 1439 m, and
 252 depths are comprised between 10 m and 513 m has been created. The density
 253 contrast $\Delta\rho$ is variable with depth and also horizontally: two sectors dividing the
 254 profile at the middle, the first one with $\Delta\rho = -580 \text{ kg m}^{-3}$ between depths from
 255 0 m to 100 m, and $\Delta\rho = -540 \text{ kg m}^{-3}$ for depths greater than 150 m ($\Delta\rho$ varies
 256 linearly between 100 m, and 150 m), and the second one with $\Delta\rho = -600 \text{ kg m}^{-3}$
 257 between depths from 0 m to 110 m, and $\Delta\rho = -570 \text{ kg m}^{-3}$ for depths greater than
 258 150 m ($\Delta\rho$ varies linearly between 110 m, and 150 m). Then a set of 99 points
 259 near uniformly distributed, and whose heights coincide with the rectangles top
 260 sides were generated. For this points the gravity anomaly corresponding to the
 261 subsoil model was generated, and then contaminated with white noise distributed

262 as $N(0, 0.25)$ mGal. Finally, a linear regional anomaly was added to each point
 263 following the trend

$$\Delta g^t = A_1(l - l_r) + A_0, \quad (6)$$

264 where $A_1 = 1.2 \cdot 10^{-3}$ mGal m $^{-1}$, $A_0 = -99.042$ mGal, $l_r = 10\,798.699$ m, and l is
 265 the position in the profile of each point.

266 The previous configuration was employed, as it was explained, for the gravity
 267 signal generation. But for the inversion a reduced model was used in order to
 268 mimic a real situation, i. e., in a real application the subsoil model is always an
 269 idealized and simplified version of a real environment. First of all, the subsoil
 270 model in the reduced version is composed by 51 rectangles of 500 m horizontal
 271 width, while the vertical and horizontal density contrast variations are the same as
 272 in the original model. The number of observation points used in the inversion is
 273 in this case 39, which were randomly selected from the original set of 99 points.
 274 Finally, the linear regional trend model will be estimated during the inversion.

275 For the inversion, the CP-PSO family member was selected, and three repeti-
 276 tions of the algorithm were combined using in each one a swarm of 200 models,
 277 and performing in each case 100 iterations, i. e., a total of 60 000 models were gen-
 278 erated. The user is strongly encouraged to read the GRAVPSO2D reference manual
 279 in order to obtain an extended discussion about the behavior of the different PSO
 280 family members and about the different approaches to perform an inversion.

281 For the filtering step, a window of width 5 elements was selected, being all
 282 the coefficients of value 1. Two passes of the filter were employed, because it
 283 was observed that in order to obtain smooth results (and in this synthetic exam-
 284 ple this is the kind of the sediments-basement interface) it is more convenient to
 285 use a narrow window combined with two passes instead of a single pass with a

286 wider filtering window. Also borehole information as absolute constraints were
 287 used, considering semi fixed (with a 10 m freedom) the depths of three rectangles
 288 (numbers 12, 13, and 31). About the cost function computation, the L_2 norm is
 289 employed considering weights based on the inverse of the observations variances.

FIGURE B.3 HERE (TWO COLUMN WIDTH)

290 Fig. B.3 (left) shows the general results of the inversion corresponding to the
 291 best model (the one among all the generated models which produces the mini-
 292 mum cost function value, which corresponds to a 2.91 % relative misfit). This
 293 plot is generated by the `grav2d_Plot.m` script, and it is composed mainly by two
 294 parts. The upper one shows the inversion residuals corresponding to each obser-
 295 vation point, while the lower part presents a general overview of the estimated
 296 sediments-basement interface. This interface is composed, in turn, by the depths
 297 corresponding to the best model, and a range of depths comprising all generated
 298 models inside the equivalent region with relative misfit lower than a selected value
 299 by the user, 4.5 %, in this case. At this point there is a limitation related to the fil-
 300 tering step that must be taken into account. Due to border effects in filtering the
 301 rectangles close to the profile ends must be analyzed carefully, and sometimes
 302 ignored. In such rectangles, where in general the sediments depth is shallow, the
 303 border effects of the filtering step produce in many cases unrealistic results that
 304 could not match the actual basement-sediments interface.

305 Fig. B.4 presents an important plot also generated by the `grav2d_Plot.m`
 306 script. For each rectangle, this plot contains in its upper part the cumulative dis-
 307 tribution function computed using all the models inside the working equivalent
 308 region (4.5 % in this example), and in its lower part the corresponding histogram.
 309 These plots are important because the user can inspect the probability distribution

of each parameter in detail. In this case, the distribution for the rectangle number 22 is clearly unimodal with depth 491.3 m, and quasi-symmetrical. This is a more convenient way to describe the uncertainty in nonlinear inverse problems than its classical expression through the most probable value plus a standard deviation, specially when the probability is far from the normal distribution (Pallero et al., 2018). But in B.4 it can also be seen that the most probable depth according to the histogram for rectangle number 22 (491.3 m) does not match the depth deduced from the best model (497.5 m), i. e., the global best model (the one with the lowest relative misfit) is not necessarily composed by the set of the most probable depths of each individual rectangle. In this particular case, the relative difference in depths with respect to the depth from the best model is 1.25 %.

FIGURE B.4 HERE (ONE COLUMN WIDTH)

In addition to the best model, a model composed by the individual most probable depths of each rectangle is generated by `grav2d_Plot.m` and called median model. In this example, the median model has a relative misfit of 3.33 % (see Fig. B.3, right), and together with the best model and the individual histograms provides a powerful information to perform the inverse problem uncertainty assessment.

FIGURE B.5 HERE (TWO COLUMN WIDTH)

Fig. B.5 shows the CDFs and histograms corresponding to the rectangle number 15 after the inversion using absolute constraints (left) and without using absolute constraints² (right). The rectangle number 15 is situated in the neighborhood of one of the absolute constraints, but not strictly contiguous, so it is a good can-

²All the other parameters in this inversion are the same as in the case of the previous experiment.

331 didate to check the influence of this kind of constraints not only in the affected
 332 rectangles itself, but also in a small area around it. As it can be seen, in both
 333 cases the histogram presents only one maximum and a near symmetrical shape,
 334 but in the inversion with absolute constraints the estimated depth is closer to the
 335 true one than in the case of inversion without absolute constraints. So the use of
 336 absolute constraints has influence not only in the affected rectangles, but also in
 337 their neighborhood. Finally, the estimated regional trend has parameters of value
 338 $A_0 = -98.675 \text{ mGal}$, and $A_1 = 1.2117 \cdot 10^{-3} \text{ mGal m}^{-1}$, presenting their corre-
 339 sponding histograms (not shown here) only one mode.

340 Figs. [B.3](#), [B.4](#), and [B.5](#) show, together with the estimated model, the true
 341 model (green line). As it can be shown, there are differences between it and the
 342 best and median models. All these differences are a consequence of the well
 343 known characteristics of inverse problems, i. e., their inherent non-uniqueness in
 344 the case of potential field based methods, the presence of noise in observations
 345 ([Fernández-Martínez et al., 2014a,b](#)), the always finite number of observations,
 346 the idealization of the model, which is in all cases a simplification of the reality,
 347 etc. All these sources of uncertainty make the task of the inverse problems not
 348 only to find the *best* model, considered as the one that adjusts the observations
 349 with minimum misfit, but a task of determination of a collection of models that are
 350 compatible at a certain level of error with all the prior information (observations,
 351 previous models, particular information of a specific parameter, etc.) at a disposal
 352 ([Scales and Snieder, 2000](#); [Tarantola, 2006](#)).

353 **7. Real example**

354 An application of GRAVPSO2D package for the inversion of observed gravity
 355 data is provided in this section. For more reliability with our previous works
 356 describing the theoretical aspects of the inversion scheme (Pallero et al., 2015;
 357 Fernández-Martínez et al., 2017) we provide here the original data corresponding
 358 to the gravity profile already discussed in these papers. In addition, with the aim
 359 at giving more replicable examples for users we have also extended this dataset
 360 with 3 other available gravity profiles also acquired during the same survey.

361 This dataset, acquired from a gravity survey carried out in the Atacama Desert
 362 (north Chile) by Gabalda et al. (2005), with the purpose of the basement relief
 363 of a sedimentary basin estimation, where irregular sediment thickness was sus-
 364 pected (presence of paleo-valleys). This region of central Andes (see Fig. B.6 for
 365 a general overview) is characterized by these continental sediments, known as the
 366 Atacama Gravels formation, derived from the Andes mountains' erosion, and de-
 367 posited in a central depression formed during the built up of the Andean system in
 368 response to the subduction of the oceanic Nazca plate beneath the South American
 369 continent (Mortimer, 1973; Riquelme, 2003). These sediments deposited on the
 370 western flank of the Andean system in El Salado valley are composed of low den-
 371 sity materials (fluvial gravels, sand and clays intercalated with ignimbrite layers
 372 (Cornejo et al., 1993)). As described in Nalpas et al. (2008), the Atacama Grav-
 373 els preserved along of the Río Salado catchment represent the infill of a drainage
 374 system of paleo-valleys converging to a canyon outlet open towards the Pacific
 375 Ocean (see Fig. B.7, dash line with arrow), indicating exoreic conditions just be-
 376 fore sedimentation. The preservation of the Atacama Gravels was related to a fall
 377 of fluvial transport capacity (limiting the mass transfer to the ocean and initiat-

378 ing the sedimentation) consecutive to a progressive climatic shift towards aridity
 379 during the Miocene. Field observations suggest that the thickness of the Atacama
 380 Gravels may reach around 150 m to 200 m in the Central Depression, and up to
 381 500 m in the “Pampa del Inca” paleovalley north of Potrerillos in the Domeyko
 382 Cordillera (Nalpas et al., 2008).

FIGURE B.6 HERE (TWO COLUMN WIDTH)

383 The density contrast sediments-basement has been estimated at around $\Delta\rho =$
 384 -800 kg m^{-3} (Gabalda et al., 2005). This high density contrast and the well pre-
 385 served nature of these basins, due to the arid climatic conditions in this region,
 386 make the Atacama Gravels formation a suitable candidate for basement relief es-
 387 timation via the gravity inverse problem. Moreover, two observable contacts along
 388 the El Salado valley between the dense substratum and the low density sedimen-
 389 tary filling (Figs. B.6 and B.7, red stars) provide valuable information for the
 390 gravity data inversion interpretation. Details on the gravity and GPS data acquisi-
 391 tion and processing performed according to the state-of-the-art for precise gravity
 392 surveys can be found in Gabalda et al. (2003, 2005).

FIGURE B.7 HERE (TWO COLUMN WIDTH)

393 The dataset is composed of four gravity profiles acquired in uneven topogra-
 394 phy area with elevations ranges between 800 m to 2400 m (see location of the 4
 395 profiles on Figs. B.6, and B.7). Three of them (P1, P2, and P3) have an orienta-
 396 tion W-E and an average altitude between 1200 m and 1500 m, while the fourth
 397 one (P4) shows an orientation mainly NW-SE and an average altitude of about
 398 2100 m (in any case, all profiles present an ascending topography eastward). The
 399 number of observed gravity measurements and the lengths for each profile are
 400 respectively 52 points and 25 km for P1, 53 points and 31 km for P2, 51 points

and 18 km for P3, and 32 points and 14 km for P4. The uncertainties of gravity and height data are estimated to be better than 20 μGal and 5 cm respectively. The interpreted final gravity values (complete Bouguer anomalies) include terrain corrections computed using a 90 m resolution topographic model.

In order to apply GRAVPSO2D to the observed profiles, we have used in all cases the CP-PSO family member, a swarm of 200 models with 200 iterations, and 3 repetitions were combined, which means that a total of 120 000 generated models for each profile inversion. The L_2 norm was used for the cost function evaluation, and two passes of a 3-element filter window with coefficients equal to 1 was applied. In all cases, a fixed density contrast sediments-basement of $\Delta\rho = -800 \text{ kg m}^{-3}$ was employed accordingly to previous estimations ([Gabalda et al., 2005](#)). The subsoil for each profile has been discretized into vertical rectangles of width corresponding to the mean separation of the observed gravity measurements. We thus obtain, 52 rectangles of width equal to 490 m for P1, 53 rectangles of width equal to 550 m for P2, 52 rectangles of width 360 m for P3 and 33 rectangles of width 420 m for P4. A first regional trend approximation is automatically subtracted from the observed Bouguer anomaly profile with the objective of isolate the residual gravity anomaly. The final regional trend (first order polynomial was chosen) is automatically estimated during the inversion process for removing the long wavelength gravity signal produced by the regional gravity (here mostly related with the deep crustal root of the Andes). In our case, the residual signal is thus supposed to be generated by the sedimentary filling of the Atacama Gravels formation in a local pre-existing morphological basin. The results of the inversion process are discussed hereafter.

[FIGURE B.8 HERE \(TWO COLUMN WIDTH\)](#)

425 Fig. B.8 shows the median estimated models for P1 (left), and P2 (right), to-
 426 gether with the 5% relative error equivalent region. In the case of P1, the profile
 427 shows two sub-basins, separated at approximately a length of 15 km along the pro-
 428 file by an outcropped basement observable in the field. The westwards sub-basin
 429 presents a maximum depth of 100 m with limits for the 5% equivalent region be-
 430 tween 92 m, and 108 m. The eastwards sub-basin shows a maximum depth of
 431 93 m with limits for the 5% equivalent region between 86 m, and 100 m. Fig. B.11
 432 (left and center) shows the cumulative distribution functions and the correspond-
 433 ing histograms for the two described rectangles corresponding to the maximum
 434 thickness. In P2 a deeper filling is observed in the first half of the profile, where
 435 the maximum depth reaches 227 m, with limits for the 5% equivalent region be-
 436 tween 196 m and 256 m. Fig. B.11 (right) shows the cumulative distribution func-
 437 tion and the corresponding histogram for this deepest point. As it can be seen,
 438 although the depth amplitude for the 5% equivalent region in this case is appar-
 439 ently wide (around 60 m), the histogram shows there is a clear maximum between
 440 depths 220 m and 230 m, so this region contains the maximum probability for the
 441 rectangle's depth.

FIGURE B.9 HERE (TWO COLUMN WIDTH)

442 Fig. B.9 shows the median estimated models for P3 (left), and P4 (right), to-
 443 gether with the 5% relative error equivalent region. In the case of P3, the profile
 444 shows an irregular basin bottom topography, with a shallow region around a dis-
 445 tance of 7 km from the initial point that divides the profile in two sub-basins. The
 446 westwards sub-basin presents a maximum depth of about 109 m with limits for the
 447 5% equivalent region between 96 m, and 122 m. The eastwards sub-basin shows
 448 a maximum depth of 110 m with limits for the 5% equivalent region between

449 100 m, and 121 m. Fig. B.12 (left and center) shows the cumulative distribution
 450 functions and the corresponding histograms for the two described rectangles. In
 451 P4 the deepest region corresponds roughly to the center of the profile, where the
 452 maximum depth reaches around 322 m, being the deepest point in the four pro-
 453 files. The limits for the 5% equivalent region are between 300 m, and 344 m.
 454 Fig. B.12 (right) shows the cumulative distribution function and the correspond-
 455 ing histogram for the rectangle. About the estimated regional trend, all profiles
 456 present a slope of value $\sim -3.26 \text{ mGal km}^{-1}$ (the adjusted values corresponding to
 457 the median models are $-3.35 \text{ mGal km}^{-1}$, $-3.23 \text{ mGal km}^{-1}$, $-3.26 \text{ mGal km}^{-1}$,
 458 and $-3.23 \text{ mGal km}^{-1}$ for profiles P1, P2, P3, and P4 respectively). Fig. B.13
 459 shows the original and residual anomaly, as well as the adjusted trend for the
 460 P1 (left), and P2 (right) profiles, while Fig. B.14 represents the same data for the
 461 P3 (left), and P4 (right) profiles.

462 In addition to the geological constraints given on the termination of the sed-
 463 imentary filling (outcropping basement) along the surveyed gravity profiles, we
 464 also have direct field observations of the actual thickness of the Atacama Gravels
 465 near the profiles P2 and P4 revealed by the erosion of the Río Salado, which allows
 466 to see locally the altitude of the base of the gravels (see Figs. B.6, and B.7, red
 467 stars). These deposits correspond to a sedimentary layer with a variable thickness,
 468 moderate in the central depression (100 m to 200 m) and more important upstream
 469 for the paleovalleys, which reach the Cordillera of Domeyco (going up to 500 m),
 470 like the “Pampa del Inca” paleovalley, north of Potrerillos (Nalpas et al., 2008).

471 For the P4 profile the “Quebrada El Salado” completely intersects the Atacama
 472 Gravels NE of the profile, a little upstream of the paleovalley of the “Pampa del
 473 Inca”, where the maximum thickness of the Graves of Atacama is about 360 m

474 (base at 1820 m, top at 2180 m). This value in the field is entirely in agreement
 475 with the thickness deduced from the inversion of the P4 profile which is 322 m
 476 (see Figs. B.9, right, and B.12, right), about 40 m less which corresponds to the
 477 gradual decrease in the thickness of the Atacama Gravels on along the paleovalley
 478 towards the central depression.

479 For the P2 profile the “Quebrada El Salado” cuts the Atacama Gravels near the
 480 western end of the El Salvador runway, where the maximum observed thickness of
 481 the Graves of Atacama is about 70 m (base at 1425 m, and top at 1495 m). As the
 482 point is located on the southern edge of the paleovalley coming from El Salvador,
 483 it is expected to have a slightly smaller thickness compared to the value of the
 484 profile, around 80 m, which is more in the axis of this paleovalley.

485 **8. Conclusions**

486 In this paper GRAVPSO2D, a Matlab software for 2D gravity inversion in sed-
 487 imimentary basins using the Particle Swarm Optimization algorithm has been pre-
 488 sented. This software represents the first effort to provide the scientific community
 489 with a tool based on the PSO for this particular problem. GRAVPSO2D is freely
 490 available and includes an exhaustive reference manual where all the details related
 491 to the input data, file formats, and output results are exposed and analyzed.

492 It is of particular importance for results interpretation the analysis of the pos-
 493 terior probability distributions of the parameters, an important task that can be ac-
 494 complished with the help of the powerful and smart ability of the PSO algorithm
 495 for sampling the parameters space. We showed its application to sedimentary
 496 basin relief estimation in synthetic and real cases.

497 The real test case presented in this paper contains a dataset of various profiles

498 corresponding to different basin geometries and depths. This dataset acquired in
 499 a context of uneven topography and of significant regional gravity anomaly also
 500 represent a standard gravity dataset that will enable the user to better handle the in-
 501 version and the parameterization taking into account the actual terrain topography
 502 and the regional trend. It can be concluded that GRAVPSO2D is a powerful soft-
 503 ware to invert and assess the uncertainty of the solution in this kind of problems
 504 via a whole family of PSO optimizers.

505 **9. Computer code availability**

506 The source code of GRAVPSO2D will be available free of charge in the BGI's
 507 webpage (<http://bgi.obs-mip.fr/>), and in <https://github.com/jgpallero/grav-psd-2d>.
 508

509 **10. Declaration of competing interest**

510 The authors declare that they have no known competing financial interests nor
 511 personal relationships that could have appeared to influence the work reported in
 512 this paper.

513 **11. Acknowledgments**

514 JLGP acknowledges the support of the GET (Université de Toulouse, CNRS,
 515 IRD, CNES), the Bureau Gravimétrique International (BGI), **and CNES**, that al-
 516 lowed him to develop part of this research in Toulouse during **two research stays**
 517 **in 2018 and 2019 (work supported by CNES, CNRS and IRD)**. He also acknowl-
 518 edges the support of the Universidad Politécnica de Madrid through a *Programa*
 519 *Propio de Movilidad* grant **in 2018**.

520 **Appendix A. Gravity attraction due to a constant density rectangle over an
521 exterior point**

522 Let a rectangle of density ρ , defined by the coordinates (see Fig. B.10) x mini-
523 mum x_m , x maximum x_M , z of top side z_t , and z of bottom side z_b . The gravitational
524 attraction generated by this polygon at an arbitrary point $P(x, y)$ is (Barbosa and
525 Silva, 1994; Telford et al., 1976)

$$\begin{aligned} F &= F(x, z, x_m, x_M, z_t, z_b, \rho) \\ &= G\rho \left[A \ln \frac{A^2 + D^2}{A^2 + C^2} - B \ln \frac{B^2 + D^2}{B^2 + C^2} \right. \\ &\quad - 2C \left(\arctan \frac{A}{C} - \arctan \frac{B}{C} \right) \\ &\quad \left. + 2D \left(\arctan \frac{A}{D} - \arctan \frac{B}{D} \right) \right], \end{aligned} \quad (\text{A.1})$$

526 where $A = x - x_m$, $B = x - x_M$, $C = z - z_t$, $D = z - z_b$, and G is the Newton's
527 constant.

FIGURE B.10 HERE (ONE COLUMN WIDTH)

528 **Appendix B. Additional figures**

529 In this appendix some auxiliary figures referred in section 7 are shown.

FIGURE B.11 HERE (TWO COLUMN WIDTH)

FIGURE B.12 HERE (TWO COLUMN WIDTH)

FIGURE B.13 HERE (TWO COLUMN WIDTH)

FIGURE B.14 HERE (TWO COLUMN WIDTH)

530 **References**

- 531 Al-Chalabi, M., 1971. Some studies relating to non uniqueness in gravity
 532 and magnetic inverse problems. *Geophysics* 36, 835–855. doi:[10.1190/1.1440219](https://doi.org/10.1190/1.1440219).
- 534 Barbosa, V.C.F., Silva, J.B.C., 1994. Generalized compact gravity inversion. *Geo-*
 535 *physics* 95, 57–68. doi:[10.1190/1.1443534](https://doi.org/10.1190/1.1443534).
- 536 Barbosa, V.C.F., Silva, J.B.C., Medeiros, W.E., 1997. Gravity inversion of base-
 537 ment relief using approximate equality constraints on depths. *Geophysics* 62,
 538 1745–1757. doi:[10.1190/1.1444275](https://doi.org/10.1190/1.1444275).
- 539 Barbosa, V.C.F., Silva, J.B.C., Medeiros, W.E., 1999. Gravity inversion of a dis-
 540 continuous relief stabilized by weighted smoothness constraints on depth. *Geo-*
 541 *physics* 64, 1429–1437. doi:[10.1190/1.1444647](https://doi.org/10.1190/1.1444647).
- 542 Blakely, R.J., 1995. Potential Theory in Gravity and Magnetic Applications. Cam-
 543 bridge University Press.
- 544 Boschetti, F., Dentith, M., List, R., 1997. Inversion of potential field data by
 545 genetic algorithms. *Geophysical Prospecting* 45, 461–478. doi:[10.1046/j.1365-2478.1997.3430267.x](https://doi.org/10.1046/j.1365-2478.1997.3430267.x).
- 547 Bott, M.H.P., 1960. The use of rapid digital computing methods for direct gravity
 548 interpretation of sedimentary basins. *Geophysical Journal of the Royal Astro-*
 549 *nomical Society* 3, 63–67. doi:[10.1111/j.1365-246X.1960.tb00065.x](https://doi.org/10.1111/j.1365-246X.1960.tb00065.x).
- 550 Brocher, T.M., 2005. A Regional View of Urban Sedimentary Basins in North-
 551 ern California Based on Oil Industry Compressional-Wave Velocity and Den-

- 552 sity Logs. Bulletin of the Seismological Society of America 95, 2093–2114.
- 553 doi:[10.1785/0120050025](https://doi.org/10.1785/0120050025).
- 554 Chakravarthi, V., Sundararajan, N., 2007. 3D gravity inversion of basement relief–
 555 A depth-dependent density approach. Geophysics 72, 123–132. doi:[10.1190/1.2431634](https://doi.org/10.1190/1.2431634).
- 557 Chen, Z., Zhang, X.M.S., 2015. 3D gravity interface inversion constrained by a
 558 few points and its GPU acceleration. Computers and Geosciences 84, 20–28.
 559 doi:[10.1016/j.cageo.2015.08.002](https://doi.org/10.1016/j.cageo.2015.08.002).
- 560 Cornejo, P., Mpodozis, C., Ramírez, C.F., Tomlinson, A.J., 1993. Estudio Ge-
 561 ológico de la región de El Salvador y Potrerillos. Informe Registrado IR 93-1.
 562 Servicio Nacional de Geología y Minería. Santiago de Chile.
- 563 Dobrin, M.B., 1960. Introduction to geophysical prospecting. 2 ed., McGraw-
 564 Hill.
- 565 Ekinci, Y.L., Balkaya, Ç., Göktürkler, G., Özyalın, Ş., 2020. Gravity data in-
 566 version for the basement relief delineation through global optimization: a case
 567 study from the Aegean Graben System, western Anatolia, Turkey. Geophysical
 568 Journal International doi:[10.1093/gji/ggaa492](https://doi.org/10.1093/gji/ggaa492).
- 569 Essa, K.S., Elhussein, M., 2018. PSO (Particle Swarm Optimization) for In-
 570 terpretation of Magnetic Anomalies Caused by Simple Geometrical Struc-
 571 tures. Pure and Applied Geophysics 175, 3539–3553. doi:[10.1007/s00024-018-1867-0](https://doi.org/10.1007/s00024-018-1867-0).
- 573 Fernández-Álvarez, J.P., Fernández-Martínez, J.L., García-Gonzalo, E.,
 574 Menéndez-Pérez, C.O., 2006. Application of the particle swarm optimization

- 575 algorithm to the solution and appraisal of the vertical electrical sounding in-
 576 verse problem, in: 10th Annual Conference of the International Association of
 577 Mathematical Geology (IAMG '06), Liège, Belgium.
- 578 Fernández-Martínez, J.L., Fernández-Muñiz, Z., Pallero, J.L.G., Bonvalot, S.,
 579 2017. Linear geophysical inversion via the discrete cosine pseudo-inverse: ap-
 580 plication to potential fields. *Geophysical Prospecting* 65, 94–111. doi:[10.1111/1365-2478.12548](https://doi.org/10.1111/1365-2478.12548).
- 582 Fernández-Martínez, J.L., Fernández-Muñiz, Z., Pallero, J.L.G., Pedruelo-
 583 González, L.M., 2013. From Bayes to Tarantola: New insights to understand
 584 uncertainty in inverse problems. *Journal of Applied Geophysics* 98, 62–72.
 585 doi:[10.1016/j.jappgeo.2013.07.005](https://doi.org/10.1016/j.jappgeo.2013.07.005).
- 586 Fernández-Martínez, J.L., García-Gonzalo, E., 2009. The PSO family: deduction,
 587 stochastic analysis and comparison. *Swarm Intelligence* 3, 245–273. doi:[10.1007/s11721-009-0034-8](https://doi.org/10.1007/s11721-009-0034-8).
- 589 Fernández-Martínez, J.L., García-Gonzalo, E., 2012. Stochastic Stability and
 590 Numerical Analysis of Two Novel Algorithms of PSO Family: PP-PSO and
 591 RR-PSO. *International Journal on Artificial Intelligence Tools* 21, 20 pages.
 592 doi:[10.1142/S0218213012400118](https://doi.org/10.1142/S0218213012400118).
- 593 Fernández-Martínez, J.L., García-Gonzalo, E., Fernández-Álvarez, J.P., 2008.
 594 Theoretical analysis of particle swarm trajectories through a mechanical anal-
 595 ogy. *International Journal of Computational Intelligence Research* 4, 93–104.
 596 doi:[10.5019/j.ijcir.2008.129](https://doi.org/10.5019/j.ijcir.2008.129).

- 597 Fernández-Martínez, J.L., García-Gonzalo, E., Fernández Álvarez, J.P., Kuzma,
 598 H.A., Menéndez Pérez, C.O., 2010a. PSO: A powerful algorithm to solve geo-
 599 physical inverse problems. Application to a 1D-DC resistivity case. Journal of
 600 Applied Geophysics 71, 13–25. doi:[10.1016/j.jappgeo.2010.02.001](https://doi.org/10.1016/j.jappgeo.2010.02.001).
- 601 Fernández-Martínez, J.L., García-Gonzalo, E., Naudet, V., 2010b. Particle swarm
 602 optimization applied to solving and appraising the streaming-potential inverse
 603 problem. Geophysics 75, WA3–WA15. doi:[10.1190/1.3460842](https://doi.org/10.1190/1.3460842).
- 604 Fernández-Martínez, J.L., Pallero, J.L.G., Fernández-Muñiz, Z., Pedruelo-
 605 González, L.M., 2014a. The effect of noise and Tikhonov's regularization in
 606 inverse problems. Part I: The linear case. Journal of Applied Geophysics 108,
 607 176–185. doi:[10.1016/j.jappgeo.2014.05.006](https://doi.org/10.1016/j.jappgeo.2014.05.006).
- 608 Fernández-Martínez, J.L., Pallero, J.L.G., Fernández-Muñiz, Z., Pedruelo-
 609 González, L.M., 2014b. The effect of noise and Tikhonov's regularization in
 610 inverse problems. Part II: The nonlinear case. Journal of Applied Geophysics
 611 108, 186–193. doi:[10.1016/j.jappgeo.2014.05.005](https://doi.org/10.1016/j.jappgeo.2014.05.005).
- 612 Fernández-Muñiz, Z., Pallero, J.L.G., Fernández-Martínez, J.L., 2020. Anomaly
 613 shape inversion via model reduction and PSO. Computers and Geosciences
 614 140, 104492. doi:[10.1016/j.cageo.2020.104492](https://doi.org/10.1016/j.cageo.2020.104492).
- 615 Gabalda, G., Bonvalot, S., Hipkin, R., 2003. CG3TOOL: An interactive com-
 616 puter program for Scintrex CG-3M gravity data processing. Computers & Geo-
 617 sciences 29, 155–171. doi:[10.1016/S0098-3004\(02\)00114-0](https://doi.org/10.1016/S0098-3004(02)00114-0).
- 618 Gabalda, G., Nalpas, T., Bonvalot, S., 2005. The Base of the Atacama Grav-
 619 els Formation (26°S, Northern Chile): First results from gravity data, in: 6th

- 620 International Symposium on Andean Geodynamics (ISAG 2005, Barcelona).
 621 Extended Abstracts, Paris, IRD. pp. 286–289.
- 622 García-Gonzalo, E., Fernández-Martínez, J.L., 2009. Design of a simple and pow-
 623 erful Particle Swarm optimizer, in: Vigo-Aguiar, J. (Ed.), Proceedings of the
 624 2009 International Conference on Computational and Mathematical Methods
 625 in Science and Engineering (volume 4), Gijón, Spain, 30 June–3 July 2009. pp.
 626 1280–1291. URL: [http://cmmse.usal.es/cmmse2018/sites/default/
 627 files/volumes/volumen4opt.pdf](http://cmmse.usal.es/cmmse2018/sites/default/files/volumes/volumen4opt.pdf).
- 628 García-Gonzalo, E., Fernández-Martínez, J.L., Cernea, A., 2014. Four-Points
 629 Particle Swarm Optimization Algorithms. Journal of Multiple-Valued Logic
 630 and Soft Computing 22, 239–266.
- 631 Granser, H., 1987. Three-dimensional interpretation of gravity data from sed-
 632 imentary basins using an exponential density-depth function. Geophysical
 633 Prospecting 35, 1030–1041. doi:[10.1111/j.1365-2478.1987.tb00858.x](https://doi.org/10.1111/j.1365-2478.1987.tb00858.x).
- 634 Hinze, W.J., von Frese, R.R.B., Saad, A.H., 2013. Gravity and Magnetic Ex-
 635 ploration. Principles, Practices and Applications. 1 ed., Cambridge University
 636 Press, Cambridge, UK.
- 637 Kennedy, J., Eberhart, R., 1995. Particle swarm optimization, in: IEEE Inter-
 638 national Conference on Neural Networks (vol. 4), Perth, WA, 27 November–1
 639 December 1995. pp. 1942–1948. doi:[10.1109/ICNN.1995.488968](https://doi.org/10.1109/ICNN.1995.488968).
- 640 Ladino, O.F., Bassrei, A., 2016. A hybrid fast 3D inversion algorithm of
 641 gravity data for basement relief definition, in: SEG Technical Program Ex-
 642 panded Abstracts 2016. SEG International Exposition and 86th Annual Meet-

- 643 ing, Dallas, USA, 16–21 October 2016. pp. 1521–1525. doi:[10.1190/segam2016-13840764.1](https://doi.org/10.1190/segam2016-13840764.1).
- 644
- 645 Li, L., Tan, J., Xie, Y., Tan, Y., Walda, J., Zhao, Z., Gajewski, D., 2019.
 646 Waveform-based microseismic location using stochastic optimization algo-
 647 rithms: A parameter tuning workflow. Computers and Geosciences 124, 115–
 648 127. doi:[10.1016/j.cageo.2019.01.002](https://doi.org/10.1016/j.cageo.2019.01.002).
- 649 Litinsky, V.A., 1989. Concept of effective density: Key to gravity determination
 650 for sedimentary basins. Geophysics 54, 1474–1482. doi:[10.1190/1.1442611](https://doi.org/10.1190/1.1442611).
- 651 Luu, K., Noble, M., Gesret, A., Belayouni, N., Roux, P.F., 2018. A parallel
 652 competitive Particle Swarm Optimization for non-linear first arrival traveltimes
 653 tomography and uncertainty quantification. Computers and Geosciences 113,
 654 81–93. doi:[10.1016/j.cageo.2018.01.016](https://doi.org/10.1016/j.cageo.2018.01.016).
- 655 Mortimer, C., 1973. The Cenozoic history of the southern Atacama Desert, Chile.
 656 Journal of the Geological Society 129, 505–526. doi:[10.1144/gsjgs.129.5.0505](https://doi.org/10.1144/gsjgs.129.5.0505).
- 657
- 658 Nalpas, T., Dabard, M.P., Ruffet, G., Vernon, A., Mpodozis, C., Loi, A., Héral,
 659 G., 2008. Sedimentation and preservation of the Miocene Atacama Gravels in
 660 the Pedernales-Chañaral Area, Northern Chile: Climatic or tectonic control?
 661 Tectonophysics 459, 161–163. doi:[10.1016/j.tecto.2007.10.013](https://doi.org/10.1016/j.tecto.2007.10.013).
- 662 Nettleton, L.L., 1976. Gravity and magnetics in oil prospecting. McGraw-Hill.
- 663 Pallero, J.L.G., Fernández-Martínez, J.L., Bonvalot, S., Fudym, O., 2015. Grav-
 664 ity inversion and uncertainty assessment of basement relief via Particle Swarm

- 665 Optimization. Journal of Applied Geophysics 116, 180–191. doi:[10.1016/j.jappgeo.2015.03.008](https://doi.org/10.1016/j.jappgeo.2015.03.008).
- 666
- 667 Pallero, J.L.G., Fernández-Martínez, J.L., Bonvalot, S., Fudym, O., 2017. 3D
668 gravity inversion and uncertainty assessment of basement relief via Particle
669 Swarm Optimization. Journal of Applied Geophysics 139, 338–350. doi:[10.1016/j.jappgeo.2017.02.004](https://doi.org/10.1016/j.jappgeo.2017.02.004).
- 670
- 671 Pallero, J.L.G., Fernández-Muñiz, M.Z., Cernea, A., Álvarez-Machancoses, Ó.,
672 Pedruelo-González, L.M., Bonvalot, S., Fernández-Martínez, J.L., 2018. Par-
673 ticle Swarm Optimization and Uncertainty Assessment in Inverse Problems.
674 Entropy 20. doi:[10.3390/e20020096](https://doi.org/10.3390/e20020096).
- 675
- 676 Parker, P.B., 1999. Genetic Algorithms and Their Use in Geophysical Problems.
677 Ph.D. thesis. University of California at Berkeley. Ernest Orlando Lawrence
678 Berkeley National Laboratory. Earth Sciences Division. URL: <http://www.osti.gov/scitech/biblio/8770/>, doi:[10.2172/8770](https://doi.org/10.2172/8770).
- 679
- 680 Parker, R.L., 1972. The Rapid Calculation of Potential Anomalies. Geophys-
681 ical Journal of the Royal Astronomical Society 31, 447–455. doi:[10.1111/j.1365-246X.1973.tb06513.x](https://doi.org/10.1111/j.1365-246X.1973.tb06513.x).
- 682
- 683 Parker, R.L., 1994. Geophysical Inverse Theory. Princeton University Press.
- 684
- 685 Pham, L.T., Oksum, E., Do, T.D., 2018. GCH_gravinv: A MATLAB-based pro-
686 gram for inverting gravity anomalies over sedimentary basins. Computers and
687 Geosciences 120, 40–47. doi:[10.1016/j.cageo.2018.07.009](https://doi.org/10.1016/j.cageo.2018.07.009).
- 688
- 689 Pick, M., Pícha, J., Vyskočil, V., 1973. Theory of the Earth's Gravity Field.
690 Elsevier.

- 688 Rao, D.B., 1990. Analysis of gravity anomalies of sedimentary basins by an
 689 asymmetrical trapezoidal model with quadratic density function. *Geophysics*
 690 55, 226–231. doi:[10.1190/1.1442830](https://doi.org/10.1190/1.1442830).
- 691 Riquelme, R., 2003. Evolution géomorphologique néogène des Andes centrales
 692 du Désert d'Atacama (Chili): interactions tectonique-érosion-climat. Ph.D. the-
 693 sis. Universidad de Chile, Université Toulouse III–Paul Sabatier.
- 694 Roshan, R., Singh, U.K., 2017. Inversion of residual gravity anomalies using
 695 tuned PSO. *Geoscientific Instrumentation, Methods and Data Systems* 6, 71–
 696 79. doi:[10.5194/gi-6-71-2017](https://doi.org/10.5194/gi-6-71-2017).
- 697 Sanyi, Y., Shangxu, W., Nan, T., 2009. Swarm intelligence optimization and its
 698 application in geophysical data inversion. *Applied Geophysics* 6, 166–174.
 699 doi:[10.1007/s11770-009-0018-x](https://doi.org/10.1007/s11770-009-0018-x).
- 700 Scales, J.A., Snieder, R., 2000. The Anatomy of Inverse Problems. *Geophysics*
 701 65, 1708–1710. doi:[10.1190/geo2000-0001.1](https://doi.org/10.1190/geo2000-0001.1).
- 702 Shaw, R., Srivastava, S., 2007. Particle swarm optimization: A new tool to invert
 703 geophysical data. *Geophysics* 72, F75–F83. doi:[10.1190/1.2432481](https://doi.org/10.1190/1.2432481).
- 704 Silva, J.B.C., Costa, D.C.L., Barbosa, V.C.F., 2006. Gravity inversion of basement
 705 relief and estimation of density contrast variation with depth. *Geophysics* 71,
 706 J51–J58. doi:[10.1190/1.2236383](https://doi.org/10.1190/1.2236383).
- 707 Silva, J.B.C., Teixeira, W.A., Barbosa, V.C.F., 2009. Gravity data as a tool
 708 for landfill study. *Environmental Geology* 57, 749–757. doi:[10.1007/s00254-008-1353-6](https://doi.org/10.1007/s00254-008-1353-6).

- 710 Singh, A., Biswas, A., 2016. Application of Global Particle Swarm Opti-
 711 mization for Inversion of Residual Gravity Anomalies Over Geological Bod-
 712 ies with Idealized Geometries. Natural Resources Research 25, 297–314.
 713 doi:[10.1007/s11053-015-9285-9](https://doi.org/10.1007/s11053-015-9285-9).
- 714 Singh, K.K., Singh, U.K., 2017. Application of particle swarm optimization for
 715 gravity inversion of 2.5-D sedimentary basins using variable density contrast.
 716 Geoscientific Instrumentation, Methods and Data Systems 6, 193–198. doi:[10.5194/gi-6-193-2017](https://doi.org/10.5194/gi-6-193-2017).
- 718 Skeels, D.C., 1947. Ambiguity in gravity interpretation. Geophysics 12, 43–56.
 719 doi:[10.1190/1.1437295](https://doi.org/10.1190/1.1437295).
- 720 Tarantola, A., 2006. Popper, Bayes and the inverse problem. Nature Physics
 721 2, 492–494. URL: <http://www.ipgp.fr/~tarantola/>, doi:[10.1038/nphys375](https://doi.org/10.1038/nphys375).
- 723 Telford, W.M., Geldart, L.P., Sheriff, R.E., Keys, D.A., 1976. Applied Geo-
 724 physics. Cambridge University Press.
- 725 Toushmalani, R., 2013a. Comparison result of inversion of gravity data of a fault
 726 by particle swarm optimization and Levenberg-Marquardt methods. Springer-
 727 Plus 2, 462. doi:[10.1186/2193-1801-2-462](https://doi.org/10.1186/2193-1801-2-462).
- 728 Toushmalani, R., 2013b. Gravity inversion of a fault by Particle Swarm Optimiza-
 729 tion (PSO). SpringerPlus 2, 315. doi:[10.1186/2193-1801-2-315](https://doi.org/10.1186/2193-1801-2-315).
- 730 Zhdanov, M.S., 2015. Inverse Theory and Applications in Geophysics. 2 ed.,
 731 Elsevier.

732 **LIST OF CAPTIONS**

- 733 Figure B.1: Two-dimensional basin model as an accretion of rectangles.
- 734 Figure B.2: Piecewise example model for vertical density contrast variation.
- 735 Figure B.3: Best model (left), and median model (right) obtained in the inver-
- 736 sion of the reduced synthetic model using absolute constraints.
- 737 Figure B.4: Cumulative distribution function (top) and histogram (bottom) for
- 738 the rectangle number 22 in the inversion of the reduced synthetic model using
- 739 absolute constraints.
- 740 Figure B.5: Cumulative distribution functions and histograms for the rect-
- 741 angle number 15 in the inversion of the reduced synthetic model using absolute
- 742 constraints (left), and without absolute constraints (right).
- 743 Figure B.6: Topography of the El Salado valley, observed gravity profiles P1
- 744 to P4, and location of the two points (red stars) of known sediments thickness.
- 745 Figure B.7: Geological background of the El Salado valley and observed grav-
- 746 ity profiles P1 to P4.
- 747 Figure B.8: Median models for P1 (left), and P2 (right). Red points were
- 748 not used in the cost function evaluation as they are situated in the outcropped
- 749 basement.
- 750 Figure B.9: Median models for P3 (left), and P4 (right). Red points were
- 751 not used in the cost function evaluation as they are situated in the outcropped
- 752 basement.
- 753 Figure B.10: Rectangle of constant density and an exterior point to it.
- 754 Figure B.11: Cumulative distribution functions and histograms corresponding
- 755 to the deepest points of the westwards (left) and eastwards (center) in the estimated
- 756 median model for the P1 profile, and the deepest point in the estimated median

757 model for the P2 profile (right).

758 Figure B.12: Cumulative distribution functions and histograms corresponding
 759 to the deepest points of the westwards (left) and eastwards (center) in the estimated
 760 median model for the P3 profile, and the deepest point in the estimated median
 761 model for the P4 profile (right).

762 Figure B.13: Gravity anomaly corresponding to the median models for the
 763 P1 (left), and P2 (right) profiles. Red points were not used in the cost function
 764 evaluation as they are situated in the outcropped basement.

765 Figure B.14: Gravity anomaly corresponding to the median models for the
 766 P3 (left), and P4 (right) profiles. Red points were not used in the cost function
 767 evaluation as they are situated in the outcropped basement.

768 **LIST OF FIGURES**

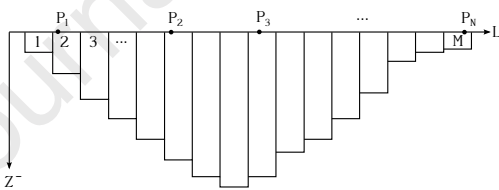


Figure B.1:

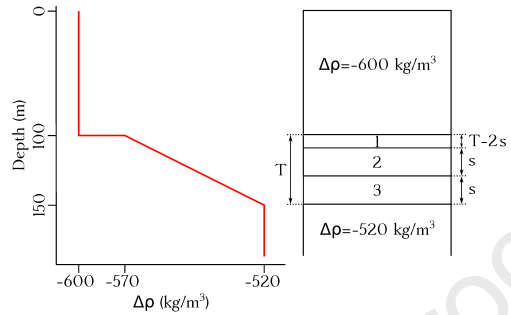


Figure B.2:

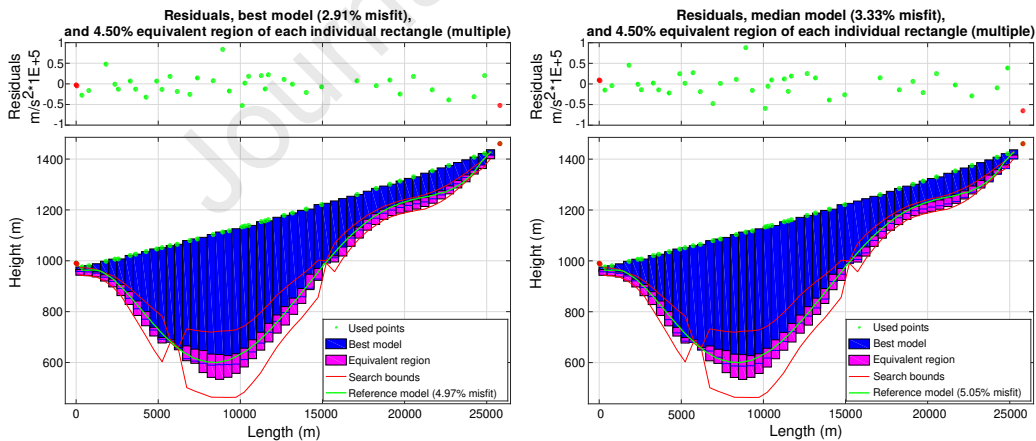


Figure B.3:

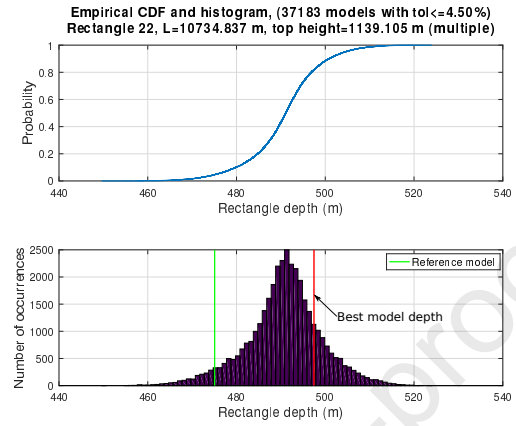


Figure B.4:

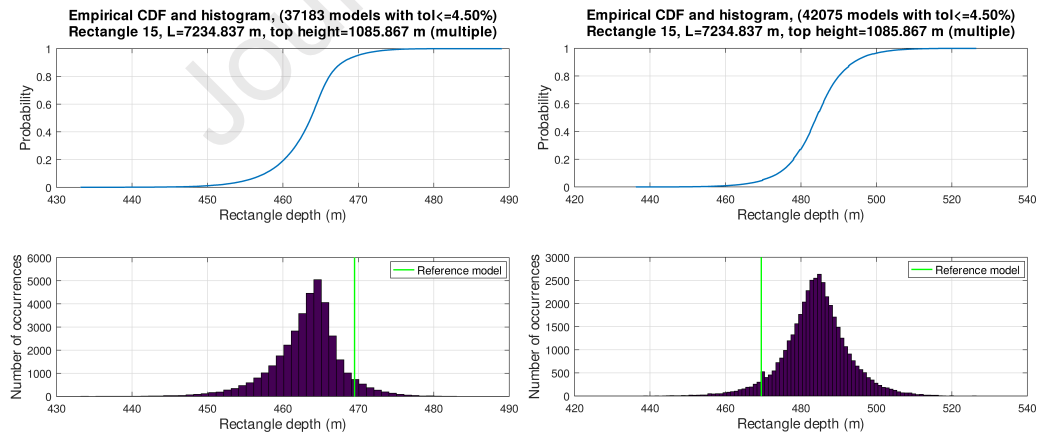


Figure B.5:

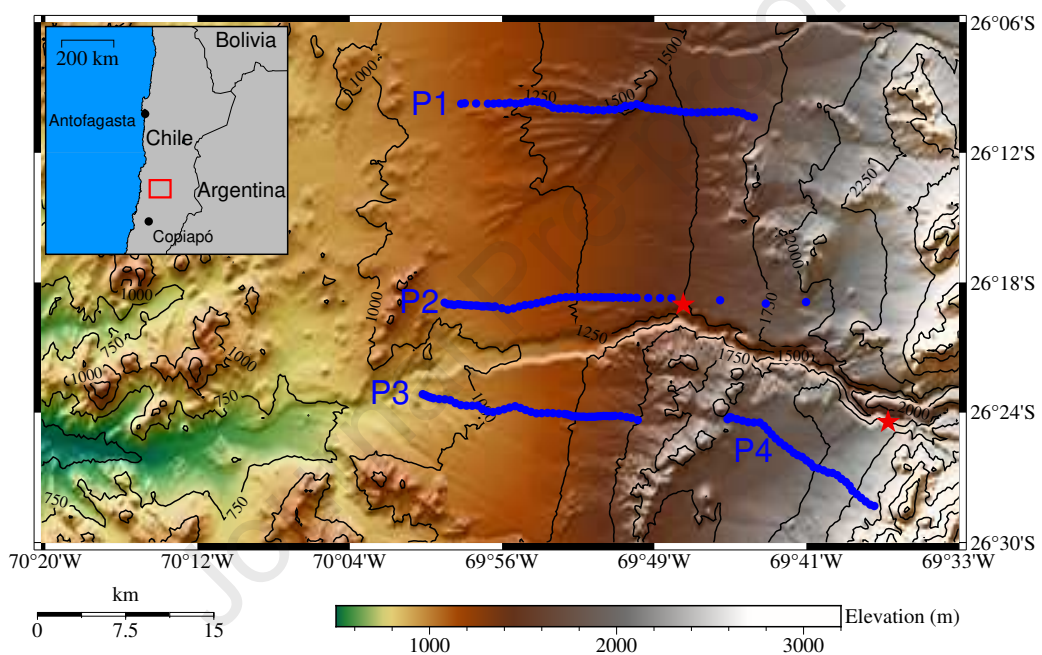


Figure B.6:

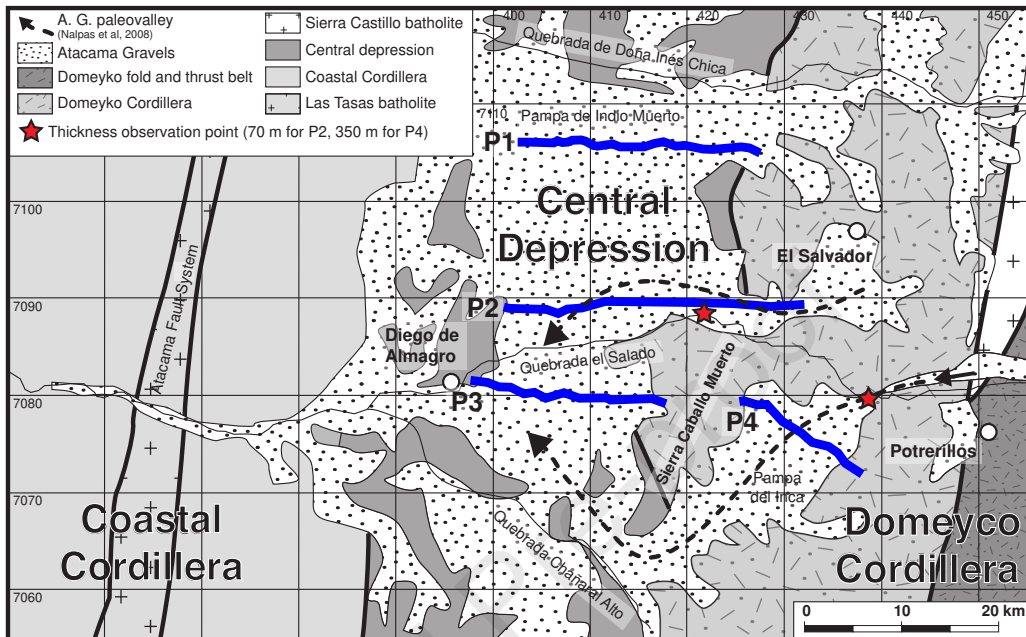


Figure B.7:

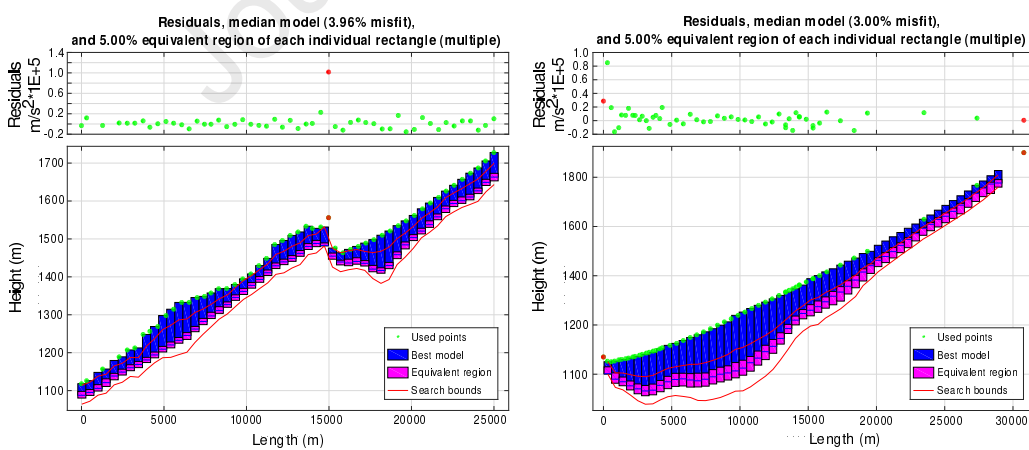


Figure B.8:

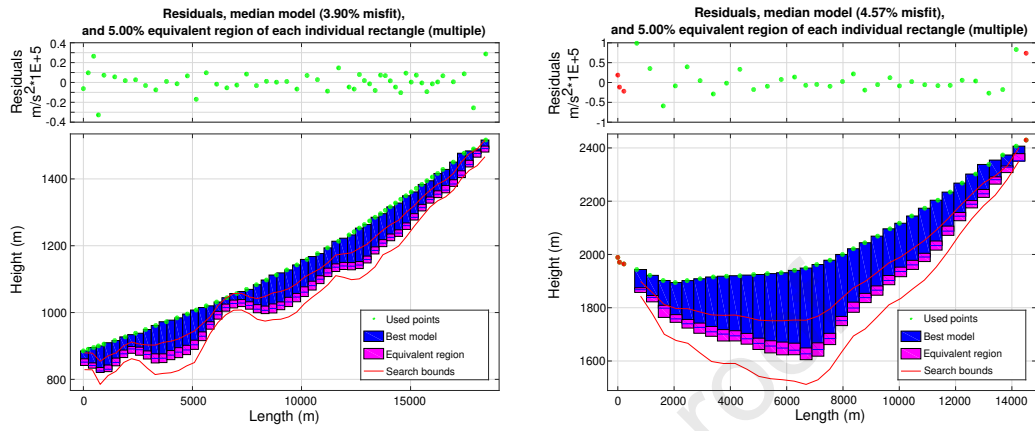


Figure B.9:

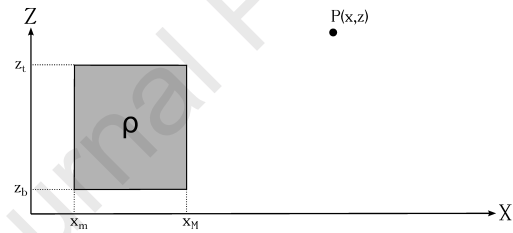


Figure B.10:

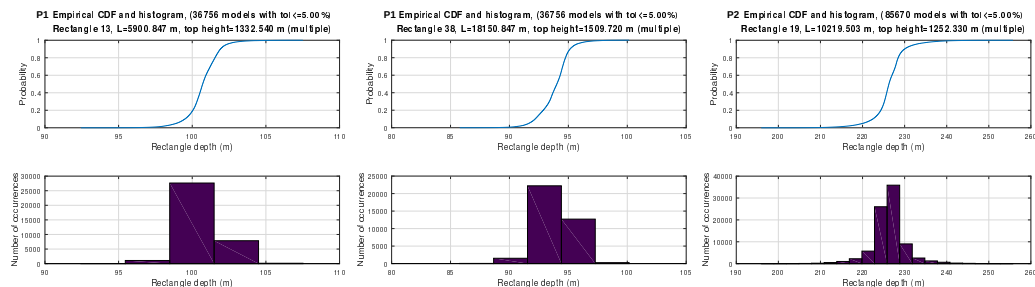


Figure B.11:

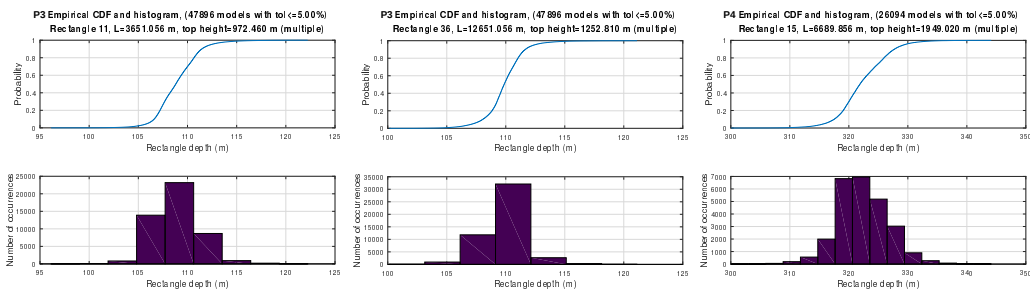


Figure B.12:

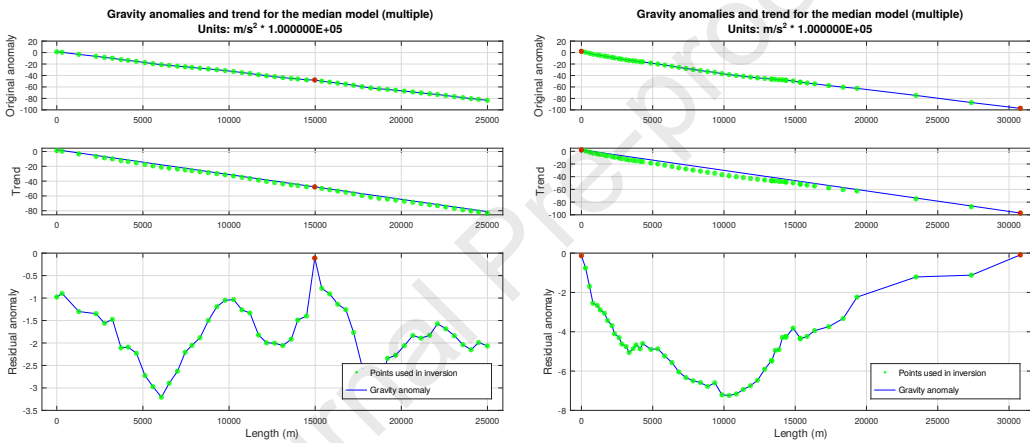


Figure B.13:

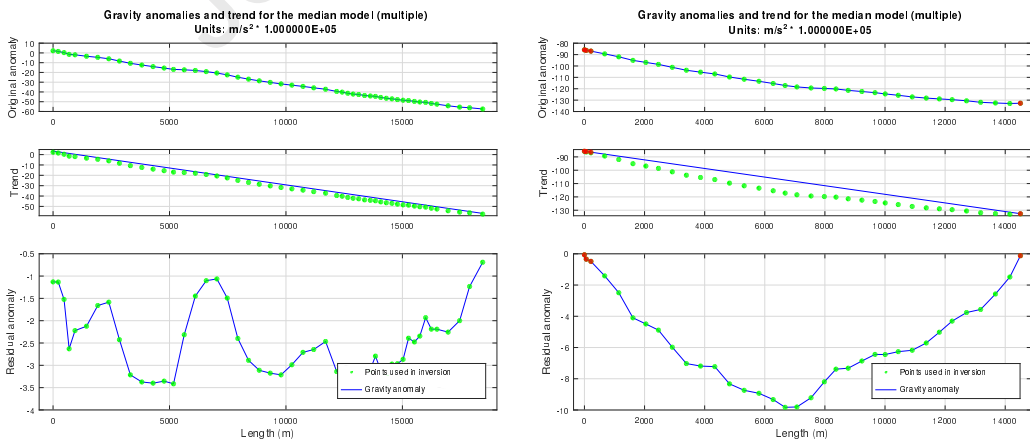


Figure B.14: